ACS APPLIED MATERIALS & INTERFACES

www.acsami.org

Research Article

Single-Crystal P2−$Na_{0.67}Mn_{0.67}Ni_{0.33}O_2$ Cathode Material with Improved Cycling Stability for Sodium-Ion Batteries

Venkat Pamidi,* Carlos Naranjo, Stefan Fuchs, Helge Stein, Thomas Diemant, Yueliang Li, Johannes Biskupek, Ute Kaiser, Sirshendu Dinda, Adam Reupert, Santosh Behara, Yang Hu, Shivam Trivedi, Anji Reddy Munnangi, Prabeer Barpanda, and Maximilian Fichtner*

Cite This: ACS Appl. Mater. Interfaces 2024, 16, 25953−25965

Read Online

ACCESS | Metrics & More | Article Recommendations | Supporting Information

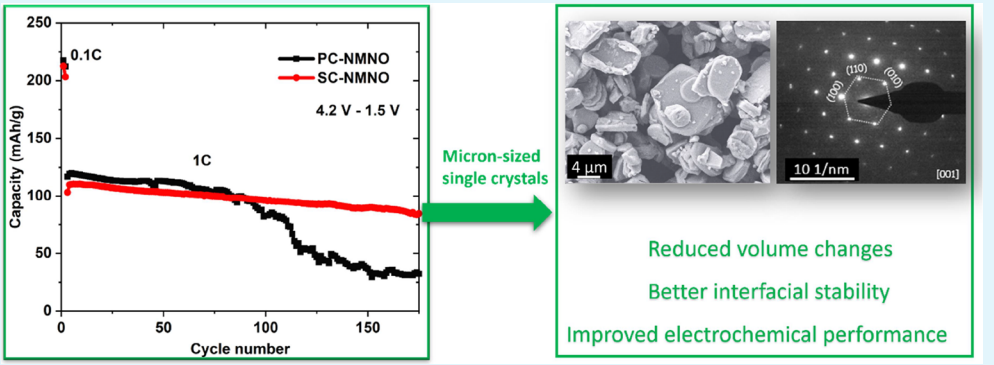

ABSTRACT: Layered oxides constitute one of the most promising cathode materials classes for large-scale sodium-ion batteries because of their high specific capacity, scalable synthesis, and low cost. However, their practical use is limited by their low energy density, physicochemical instability, and poor cycling stability. Aiming to mitigate these shortcomings, in this work, we synthesized polycrystalline (PC) and single-crystal (SC) P2-type $Na_{0.67-\delta}Mn_{0.67}Ni_{0.33}O_2$ (NMNO) cathode materials through a solid-state route and evaluated their physicochemical and electrochemical performance. The SC-NMNO cathode with a large mean primary particle size (D_{50}) of 12.7 μm was found to exhibit high cycling stability leading to 47% higher capacity retention than PC-NMNO after 175 cycles at 1C rate in the potential window 4.2−1.5 V. This could be attributed to the effective mitigation of parasitic side reactions at the electrode−electrolyte interface and suppressed intergranular cracking induced by anisotropic volume changes. This is confirmed by the lower volume variation of SC-NMNO ($\Delta V \sim 1.0\%$) compared to PC-NMNO ($\Delta V \sim 1.4\%$) upon charging to 4.2 V. Additionally, the SC-NMNO cathode displayed slightly higher thermal stability compared to PC-NMNO. Both cathodes exhibited good chemical stability against air and water exposure, thus enabling material storage/handling in the ambient atmosphere as well as making them suitable for aqueous processing. In this regard, PC-NMNO was investigated with two low-cost aqueous binders, carboxymethyl cellulose, and sodium trimetaphosphate, which exhibited higher binding strength and displayed excellent electrochemical performance compared to PVDF, which could potentially lead to significant cost reduction in electrode manufacturing.

KEYWORDS: *sodium-ion batteries, layered oxides, single-crystal cathodes, inorganic aqueous binder, sodium trimetaphosphate, thermal stability*

1. INTRODUCTION

Energy storage on a large scale necessitates abundant and sustainable base materials from uncritical sources. In this regard, sodium-ion batteries (SIBs) pose as a low-cost, highly and globally abundant complement to well-proliferated lithium-ion batteries (LIBs).[1,2] Currently, one major performance limiting factor in SIBs is the cathode material, in which layered oxides are the most widely explored class owing to their high specific capacity, ease of large-scale synthesis, and low cost.[2] Among them, P2-type $Na_{0.67}Mn_{0.67}Ni_{0.33}O_2$ (NMNO) offers a large reversible capacity and high average voltage.[3−5] However, it undergoes P2 to O2 phase transformation at a voltage higher than 4.2 V, triggering significant volume strain (ca. ∼23%), which leads to structural instability and rapid capacity fading.[6,7] This undesirable phase transition

Received: October 13, 2023
Revised: March 15, 2024
Accepted: March 18, 2024
Published: May 8, 2024

can be mitigated by employing strategies such as doping/substitution, surface modification, and microstructure engineering. For example, improved cycling stability in P2-type cathodes has been reported by doping/substitution of elements such as Mg,[8] Al,[9] Ti,[10] Cu,[11] and Fe.[12] Similarly, surface coatings such as Al_2O_3,[13] TiO_2,[14] MgO,[15] and Na_2SiO_3[16] have been reported to improve the electrochemical performance by suppressing the parasitic side reactions at the electrode/electrolyte interface. In addition, surface coating has also been shown to facilitate high voltage cycling stability by suppressing cracking/exfoliation of cathode particles.[13]

In addition, tuning particle morphology and design strategies such as core−shell structures and biphasic materials can lead to higher capacity, cycling stability, and rate capability.[17,18] In the case of LIBs, micrometer-sized single-crystal (SC) particles were demonstrated to exhibit excellent cycling stability (even at high temperatures and high voltages) as well as improved thermal stability over conventional polycrystalline (PC) particles.[19−21] The improved performance of SC cathodes has been attributed to the suppression of microcracking of particles (owing to grain boundary-free core) and reduced parasitic side reactions (due to low surface area).

In that context, our group reported micrometer-sized SC particles based on $Na_{0.7}Mn_{0.9}Mg_{0.1}O_2$ cathode materials for SIBs.[22] In parallel, Mao et al.[4] and Yang et al.[23] reported similar micrometer-sized SC particles with excellent cycling stability and high-rate capability. However, there is no comparative study of their respective PC analogues. Additionally, it should be noted that the reported nanosized SC particles[24−26] are significantly different (due to their high surface area) and do not have the above-mentioned advantages of micrometer-sized SC particles.

The development of sustainable SIBs benefits if the storage/handling of cathode materials can be done under ambient conditions. Currently, polyvinylidene fluoride (PVDF) stands out as a dominant binder for positive electrode formulation due to its good dispersion properties and high (electro)-chemical stability.[27] However, PVDF is commonly used with an organic solvent such as *N*-methyl-2-pyrrolidone (NMP), an expensive, environmentally unfriendly, toxic, and volatile solvent.[28] Additionally, PVDF recycling and NMP solvent extraction processes are also expensive, energy-intensive, and environmentally unfriendly.[29] Electrode manufacturing/solvent evaporation/recovery is estimated to account for almost 30% of the total cost of battery manufacturing.[30] In this context, aqueous binders should be harnessed for the SIBs. There are sparse reports on aqueous binder-based processing of cathode materials for SIBs, primarily due to their chemical incompatibility with moisture/water (see Table S1). Therefore, it is crucial to develop moisture-water-stable cathode materials and high-performance aqueous binders to reduce battery manufacturing costs and reduce environmental hazards.

In this work, a particle morphology engineering strategy was employed on P2-type NMNO cathode materials to synthesize particles of PC and single-crystalline morphologies using a facile solid-state method. The SC-NMNO electrode exhibited 47% higher capacity retention than PC-NMNO after 175 cycles at a 1C rate, which can be attributed to reduced parasitic side reactions and/or reduced particle surface degradation. Additionally, taking advantage of the moisture/water stability of PC-NMNO, it was evaluated with two different aqueous binders, namely, carboxymethyl cellulose (CMC) and sodium trimetaphosphate (STMP). The resulting electrodes exhibited improved cycling stability as well as rate capability compared to the PVDF-based electrode. The intrinsic ionic conductivity and higher binding strength of these aqueous binders as well as their ability to form a uniform layer on the cathode and carbon composite can be assigned to improved electrochemical performance.

2. EXPERIMENTAL SECTION

2.1. Materials Synthesis. The polycrystal and SC P2-type $Na_{0.67}Mn_{0.67}Ni_{0.33}O_2$ (PC-NMNO and SC-NMNO) cathode materials were prepared via a simple solid-state method. In a typical process, stoichiometric amounts of Na_2CO_3 (Sigma-Aldrich, purity ≥99.5%), MnO_2 (Alfa Aesar, purity 99.9%), and NiO (Alfa Aesar, purity 99%) were intimately mixed by ball-milling (at 500 rpm for 2 h). The resultant powder mixture was calcined in air at 900 °C for 15 h (with a heating rate of 5 °C/min) followed by natural cooling inside the muffle furnace (Carbolite CWF 11/13). This sample is referred to as PC-NMNO. To synthesize SC particles, PC-NMNO was again heated in air at 1050 °C for 15 h to promote grain growth. The resulting sample is denoted SC-NMNO. No additional Na precursor was added during synthesis. Both samples were stored in an argon-filled glovebox with a circulation system (O_2 and H_2O < 1 ppm). For the air stability test, 0.5 g of each cathode material was spread on a Petri dish and was stored in a fume hood for 90 days maintaining a relative humidity of ∼40% at ∼25 °C. For the water stability test, 0.5 g of each cathode material was stirred in deionized water for 4 h, followed by centrifugation at 3000 rpm for 10 min to collect the powder/paste and was dried at 90 °C for 12 h. Structural analysis was performed on the samples after the air and water stability test without further processing of the cathode materials.

2.2. Physicochemical Characterization. The phase analysis of the as-synthesized cathode materials as well as the cathode materials subjected to air and water stability tests was performed by powder X-ray diffraction (XRD) measurements using a STOE Stadi P diffractometer equipped with a Mo Kα radiation source (λ = 0.709 Å) in the transmission mode. The XRD patterns recorded between 5° < 2θ < 40° were analyzed with HighScore Plus software for preliminary phase identification followed by Rietveld refinement with FullProf software. The operando XRD study was performed on both PC-NMNO and SC-NMNO electrodes to probe the structural evolution during the initial two (dis)charge cycles at a rate of 0.1C in the potential window 4.2−1.5 V. The powder patterns were acquired in transmission mode with an STOE Stadi P diffractometer equipped with an Ag Kα radiation source (λ = 0.5594 Å). For operando XRD measurements, CR2023-type coin cells were assembled with a glass window and were cycled using a single-channel potentiostat (Biologic SP-150).

Microstructural investigation was performed by scanning electron microscopy (SEM, ZEISS Crossbeam 340) using an accelerating voltage between 2 and 10 kV. The particle size distribution was determined using a laser particle analyzer (Malvern Mastersizer 3000). The chemical composition of the as-synthesized cathode materials was investigated by inductively coupled plasma optical emission spectroscopy (ICP-OES).

Morphological and structural investigation of the pristine cathode materials was conducted using aberration-corrected high-resolution transmission electron microscopy (HRTEM) at a working voltage of 300 kV (FEI Titan 80−300). The local elemental distribution was determined using scanning TEM (STEM) together with the parallel acquisition of energy-dispersive X-ray spectroscopy (EDX) data at a working voltage of 200 kV (Thermofisher Talos 200X). For the TEM study, the samples were prepared by suspending a small amount of the cathode materials in 2 mL of ethanol using an ultrasonic bath. The suspension was deposited by drop casting on a holey carbon-coated grid.

X-ray photoelectron spectroscopy (XPS) measurements were performed with a Specs EnviroESCA unit having a monochromatic Al Kα source (1486.6 eV). Survey spectra were taken at 100 eV pass energy, and high-resolution spectra were taken at 30 eV pass energy.

https://doi.org/10.1021/acsami.3c15348
ACS Appl. Mater. Interfaces 2024, 16, 25953−25965

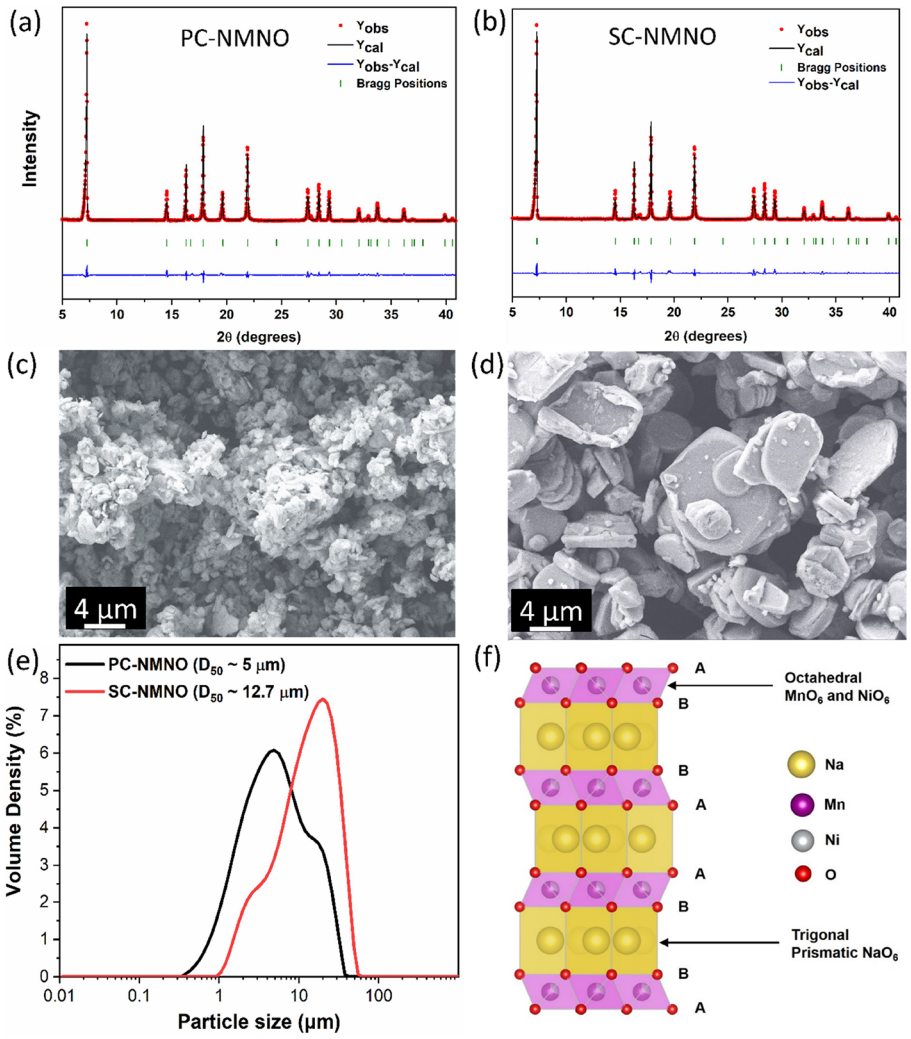

Figure 1. Structural characterization of as-prepared cathode materials. (a, b) Rietveld refined profiles based on powder XRD patterns of PC-NMNO and SC-NMNO, (c, d) representative SEM images of PC-NMNO and SC-NMNO, respectively, (e) particle size distribution measured using a laser particle analyzer (Mastersizer 3000), and (f) crystal structure of P2-type NMNO cathode material illustrated using Vesta software.

Data were analyzed with CasaXPS using a Shirley-type background and Gaussian (70%) and Lorentzian (30%) profiles. The XPS is part of PLACES/R, an autonomous research platform for accelerated electrochemical energy storage research.[31] Transmission X-ray absorption spectra (XAS) were obtained by using a laboratory device (easyXAFS300+, easyXAFS LLC). Mn and Ni K-edge spectra were collected from pellets (made by diluting with cellulose) and were compared with standard references with known oxidation states.

The binding strength of each binder was measured by a peel-test experiment. Two separate pieces of aluminum foil were attached to one another using either PVDF or aqueous binders in equal amounts (~20 mg). While one end of the aluminum foil was fixed to a table using cell tape, the opposite end of the other aluminum foil was connected to a spring-loaded thrust meter (maximum force ~10 N). Next, the meter was gradually pulled until one of the aluminum foils completely peeled off from the other foil. The reading from the spring-loaded thrust meter was taken as the adhesion force or binding strength.

2.3. Electrochemical Characterization. For electrode preparation, a slurry was prepared with the cathode active material, carbon black (Alfa Aesar, Super P, purity ≥99%), and binder in an 8:1:1 weight ratio in a minimal amount of *N*-methyl-2-pyrrolidone (NMP) (Alfa Aesar, purity: 99.5%) solvent. The slurry for the PVDF (Kynar HSV 900) binder-based electrodes was prepared using mortar and pestle inside an argon-filled glovebox by employing NMP as a solvent and was coated on aluminum foil. For aqueous binder-based electrodes, CMC (Sigma-Aldrich, medium viscosity) and STMP (Aldrich Chemistry, purity ≥95%) were used as binders. The CMC- and STMP-based slurries were prepared using a mortar and pestle in a fume hood by employing distilled water as solvent. The slurry was spread on carbon-coated aluminum foil using a doctor blade coater with a wet layer thickness of ~200 μm. Finally, the electrodes were vacuum-dried at 110 °C for 12 h, and circular disks (diameter = 12 mm) were punched out acting as working electrodes. The mass loading of the electrodes was ~5 mg.

Electrochemical performance was evaluated using Swagelok-type half cells with sodium metal as the counter electrode, two borosilicate glass fiber sheets (GF/C) as separator soaked with 60 μL of electrolyte (1 M $NaClO_4$ in propylene carbonate (PC, 98% v/v)/fluoroethylene carbonate (FEC, 2% v/v)). The cells were cycled at room temperature using a Biologic BCS-805 battery tester. Before each test, the cells were rested for 7 h. Potentiostatic electrochemical impedance spectroscopy (PEIS) was performed between 10 mHz and 10 kHz before and after cycling.

3. RESULTS AND DISCUSSION

3.1. Structural Analysis. P2-type $Na_{0.67}Mn_{0.67}Ni_{0.33}O_2$ (NMNO) was synthesized in both PC and SC forms via a simple solid-state route with the only difference being the calcination temperature. While the PC-NMNO was calcined at 900 °C, the SC-NMNO was synthesized by calcining the PC-

https://doi.org/10.1021/acsami.3c15348
ACS Appl. Mater. Interfaces 2024, 16, 25953−25965

NMNO at 1050 °C. This increased calcination temperature strategy is the most common approach in the LIBs literature to synthesize SCs.[19−21] The SC-NMNO was formed through grain growth via a grain boundary migration mechanism. The additional heating step employed for PC-NMNO at 1050 °C increases the ion mobility, which increases the rate of grain growth. The driving force for this reaction is the size difference between the adjacent grains. Since the larger grains have a lower surface area relative to their volume, they tend to consume smaller grains to reduce their surface energy.[32] As shown in Figures 1a,b and S1a,b, XRD patterns of both samples were fitted by taking $Na_{0.70}MnO_{2.05}$ (ICSD file: 00-027-0751) as a reference pattern with a hexagonal layered structure having *P*63/*mmc* symmetry. No obvious impurities or secondary phases were observed. However, a marginal shift in the (002) peak position toward lower angles was observed for both samples compared to the reference pattern, which originated due to the substitution of larger Ni^{2+} cation by Mn^{3+}/Mn^{4+} (Figure S1b). The diffraction patterns of both PC and SC were quite similar, except SC-NMNO exhibited slightly higher intensity due to a higher calcination temperature (as well as the second calcination), resulting in slightly enhanced crystallinity (see Figure S2). The crystallographic data including the calculated lattice parameters, atomic positions, and occupancies are reported in Tables S2 and S3. The NMNO framework is composed of alternate layers of TMO_2 (octahedral coordination of MnO_6 and NiO_6) and Na layers (trigonal prismatic coordination of NaO_6) with the AB BA stacking sequence (Figure 1f). The Na^+ ions occupy two distinct prismatic sites: either edge sharing or face sharing with TMO_6 octahedra.[33]

Using ICP-OES, the actual chemical compositions of the as-synthesized cathode materials were determined to be $Na_{0.53}Mn_{0.57}Ni_{0.28}O_2$ and $Na_{0.48}Mn_{0.54}Ni_{0.26}O_2$ for PC and SC samples, respectively. These measured compositions matched closely to the expected stoichiometry, except for the Na content. The reduction in Na content was due to the sodium loss/evaporation during the calcination, which can be compensated by adding additional Na content. The actual composition could be "$Na_{0.67-\delta}Mn_{0.67}Ni_{0.33}O_{2-x}$", where the symbols "$\delta$" and "$x$" account for the Na loss and oxygen vacancies, respectively. It was expected that the (002) peak of SC-NMNO sample shifts to a lower 2θ value compared to the PC-NMNO due to the loss of sodium during the additional calcination step involved in the SC preparation.[22] The loss of Na could increase the distance between MO_2 layers (thereby increasing the *d*-spacing/*c*-lattice parameter) due to the increased electrostatic repulsions between negatively charged O^- ions of MO_2 layers.[34] However, no noticeable shift was observed between the XRD patterns of PC and SC samples (see Figure S1b). The SEM measurements revealed a primary particle size in the range of a few 100 nm and a secondary particle size (D_{50}) of ∼5 μm (Figures 1c and S3) for the polycrystalline PC-NMNO, whereas SC-NMNO exhibited SCs with a mean particle size of ∼12.7 μm (Figures 1d and S4). The relative particle size distributions are shown in Figure 1e. It should be noted that the PC-NMNO did not exhibit the spherical PC form, which was reported in the literature.[5,19] The particles of SC-NMNO had a flake/plate morphology with well-defined edges, while PC-NMNO did not show well-defined secondary particles. From their particle size, the PC-NMNO is expected to have higher surface area than SC-NMNO as reported in our previous work.[22]

To validate that as-synthesized PC-NMNO and SC-NMNO cathode materials are indeed PC and single crystalline in nature, TEM investigations were performed (Figure 2). The

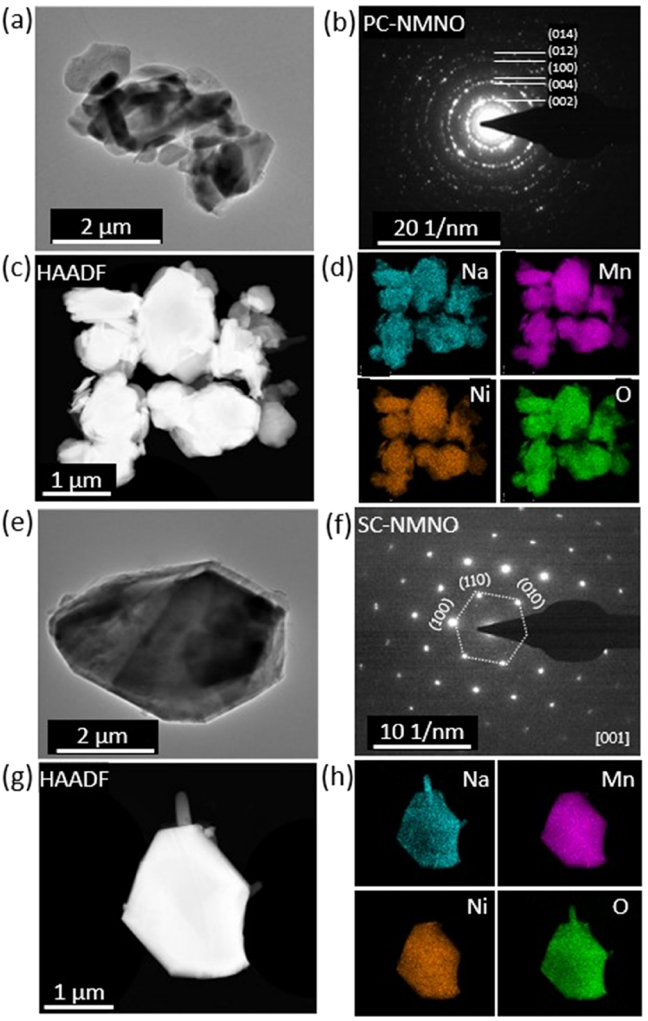

Figure 2. TEM analysis of PC-NMNO and SC-NMNO cathode materials. (a) Overview of bright-field TEM image and corresponding (b) SAED pattern, (c) high-angle annular dark-field (HAADF) stem image, and (d) corresponding EDX elemental mappings of PC-NMNO particles. (e) Overview of bright-field TEM image and corresponding (f) SAED pattern, (g) HAADF image, and (h) corresponding EDX elemental mappings of SC-NMNO.

dotted rings in the selected area electron diffraction (SAED) pattern confirmed the PC nature of PC-NMNO samples (Figure 2b). In contrast, the hexagonal dotted SAED pattern indicated a single-crystalline nature of the SC-NMNO sample (Figure 2f). Additionally, EDX elemental mappings of both samples confirmed uniform distribution of the constituent elements Na, Mn, Ni, and O, without any elemental segregation.

A majority of the sodium-layered oxide cathode materials suffer from moisture-related degradation. In this work, the bulk chemical stability of both cathode materials was investigated in an ambient atmosphere and in water. As shown in Figure S1c, the XRD patterns of both samples showed the P2 structure even after exposing to ∼40% RH (at 25 °C) for 90 days,

https://doi.org/10.1021/acsami.3c15348
ACS Appl. Mater. Interfaces 2024, 16, 25953−25965

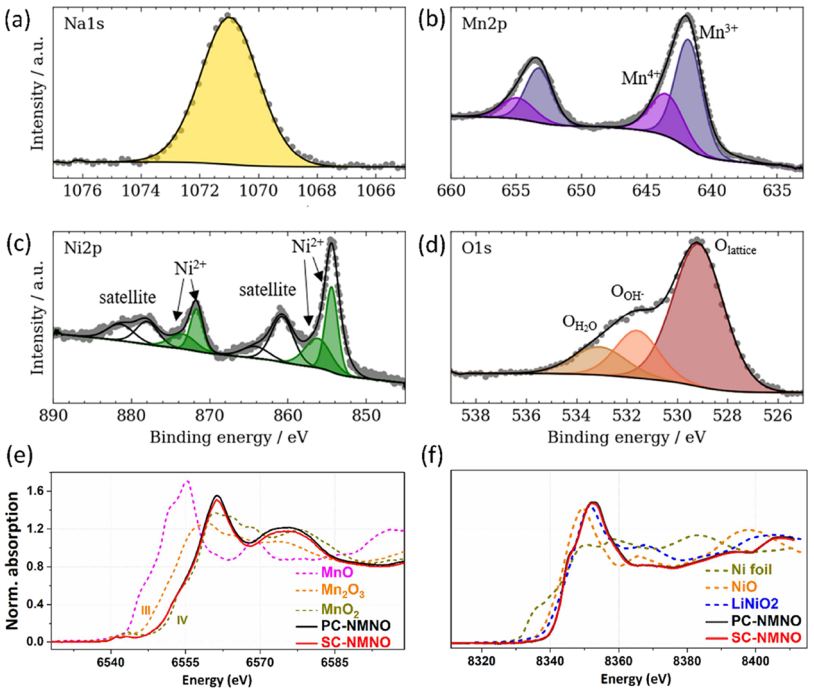

Figure 3. XPS analysis of PC-NMNO and XANES results of PC-NMNO and SC-NMNO. Deconvoluted XPS detail spectra of the (a) Na 1s, (b) Mn 2p, (c) Ni 2p, and (d) O 1s regions. (e, f) Normalized XANES spectra for the Mn K-edge and Ni K-edge for PC and SC materials. The average oxidation states of transition metals were evaluated by the "fingerprint" method with known standards, most of which are oxides with $M-O_6$ coordination.

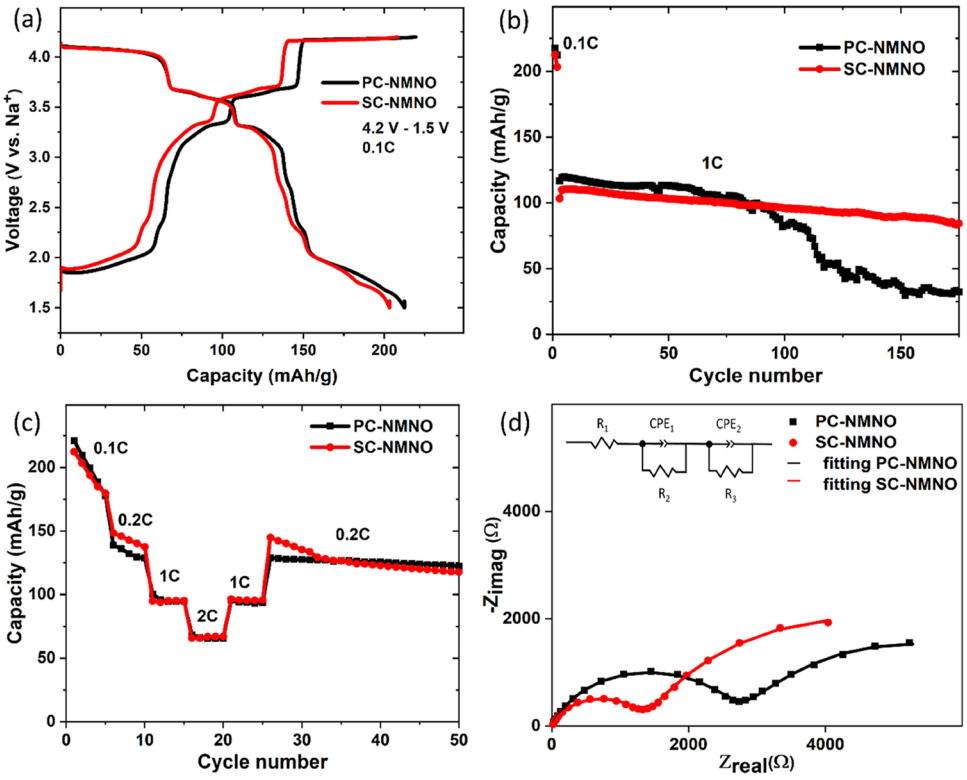

Figure 4. Electrochemical performance of PC-NMNO and SC-NMNO electrode materials in the potential window 4.2−1.5 V. (a) Second charge−discharge profiles at a rate of 0.1C, (b) cycling stability at 1C, (c) rate capability, and (d) electrochemical impedance spectra (EIS) (inset: electrochemical equivalent circuit).

indicating excellent structural stability, although PC-NMNO exhibited few additional low-intensity peaks corresponding to Na_2CO_3, NaOH, or $NaHCO_3$.[35−38] These impurities are known to create problems for electrode manufacturing due to their reaction with PVDF and an increase of the overall cell impedance due to their insulating nature.[6] The surface

https://doi.org/10.1021/acsami.3c15348
ACS Appl. Mater. Interfaces 2024, 16, 25953−25965

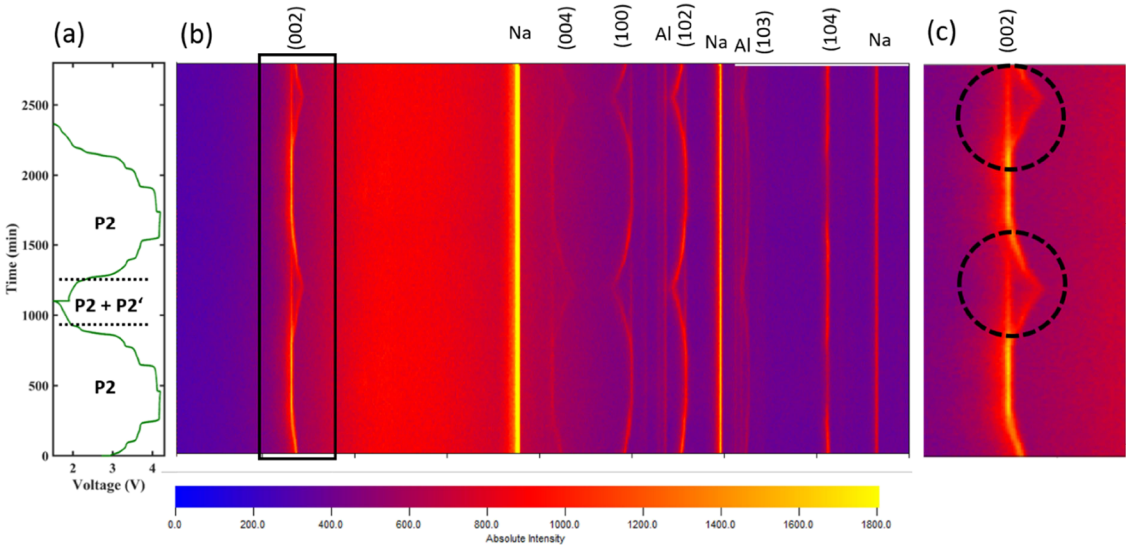

Figure 5. Structural evolution of SC-NMNO sample during initial two charge−discharge cycles. (a) Charge−discharge curve, (b) operando XRD contour plot recorded at 0.1C rate in the potential window 4.2−1.5 V, and (c) enlarged view of the (002) peak evolution.

impurities on the particles could be attributed to some of these impurity phases (see Figure S1e). In any case, the material retained the original structure after heating the air-exposed sample to 300 °C for 2 h, pointing to good structural reversibility of PC-NMNO.

In contrast, SC-NMNO showed a negligible amount of such impurities (Figure S1f). Surprisingly, both samples exhibited outstanding bulk stability in water as well, as observed from the XRD patterns in Figure S1d. No additional impurity peaks were observed. Overall, the excellent chemical stability of both compounds allows easy storage and handling under ambient conditions as well as to development of aqueous electrode processing methods, which could potentially reduce battery manufacturing costs.

Figure 3a−d displays the high-resolution XPS detail spectra of the Na 1s, Ni 2p, Mn 2p, and O 1s region of PC-NMNO. In the Na 1s region, a single peak was observed at ∼1071.0 eV corresponding to Na^+. The Mn 2p peak can be deconvoluted into two doublets (with Mn $2p_{3/2}$ peaks at 641.8 and 643.4 eV). The position of the main Mn $2p_{3/2}$ peak is usually expected for Mn species with an oxidation state of +III or +IV (or a mixture of the two). To decide between these two oxidation states, X-ray absorption near edge structure (XANES) spectra were collected at the Mn K-edge (Figure 3e). The result of this measurement points to a predominance of Mn (+IV). The Ni 2p region (Figure 3c) can be deconvoluted by two sets of doublets at 854.4 and 856.1 eV with a spin−orbit splitting of 17.3 eV assigned to Ni^{2+} oxidation state and satellites at 860.7 and 864.1 eV. The XANES spectra of the Ni K-edge (Figure 3f) show that both PC and SC exhibited similar oxidation states. Finally, the spectrum in the O 1s region (Figure 3d) was composed of three peaks at 528.7, 531.1, and 533.0 eV, which can be assigned to lattice oxygen, adsorbed hydroxides, and adsorbed water, respectively.[39] The XPS spectra of the SC-NMNO electrode are presented in the SI (Figure S5). As discussed above, the Na 1s and Mn 2p regions of the SC-NMNO electrode are similar to that of the PC-NMNO. However, the intensity of the $O_{lattice}$ peak in the O 1s region of the SC-NMNO electrode was lower than expected, possibly due to the presence of the carbon and binder in the electrode. Additionally, the local structure of PC-NMNO was further probed by Raman spectroscopy. The results and the corresponding explanation are presented in the SI (Figure S6).

3.2. Electrochemical Performance. The electrochemical performance of the PC- and SC-NMNO cathode materials was evaluated in half cells against a Na metal anode using Swagelok cells. Figure 4 shows the electrochemical performance in the potential window 4.2−1.5 V. While the (dis)charge profiles of both electrodes are similar (Figure 4a), the SC-NMNO exhibited slightly lower reversible capacity (second cycle discharge capacity) of 202 mA h/g compared to 212 mA h/g for PC-NMNO. This can be explained by the slight loss/evaporation of sodium at high temperatures during the SC synthesis step (1050 °C for SC vs 900 °C for PC). Overall, both (dis)charge profiles showed three voltage plateaus at ∼2, ∼3.6, and ∼4.16 V during charging (desodiation), like the reported literature on P2-NMNO compounds,[5,34] suggesting different mechanisms such as Na^+/vacancy ordering and/or stacking faults. The high voltage plateau at ∼4.16 V was attributed to the irreversible oxygen redox, according to the literature.[40] During discharge (sodiation), symmetrically opposite behavior was observed. However, the PC-NMNO exhibited slightly higher polarization compared to SC-NMNO (see Figure S7). Both PC-NMNO and SC-NMNO electrodes exhibited similar cycling stability up to ∼90 cycles at the 1C rate, even though SC-NMNO exhibited slightly lower capacity (Figure 4b). In the following, however, SC-NMNO retained 74% (∼83 mA h/g) of its initial capacity after 175 cycles compared to 27% (∼32 mA h/g) for PC-NMNO. Surprisingly, both PC- and SC-NMNO electrodes exhibited comparable rate capabilities at all of the rates investigated (Figure 4c). Table S1 summarizes the electrochemical performance results from the current work and compares them with the respective literature. The EIS results in Figure 4d and Table S4 demonstrate that the interfacial resistance (R_{SEI}) of the PC-NMNO is higher than that of SC-NMNO, which might be attributed to the presence of grain boundaries and small insulating surface impurities in the form of Na_2CO_3/NaOH. In contrast, the charge transfer resistance (R_{CT}) of SC-NMNO was higher than that of PC-NMNO.

https://doi.org/10.1021/acsami.3c15348
ACS Appl. Mater. Interfaces 2024, 16, 25953−25965

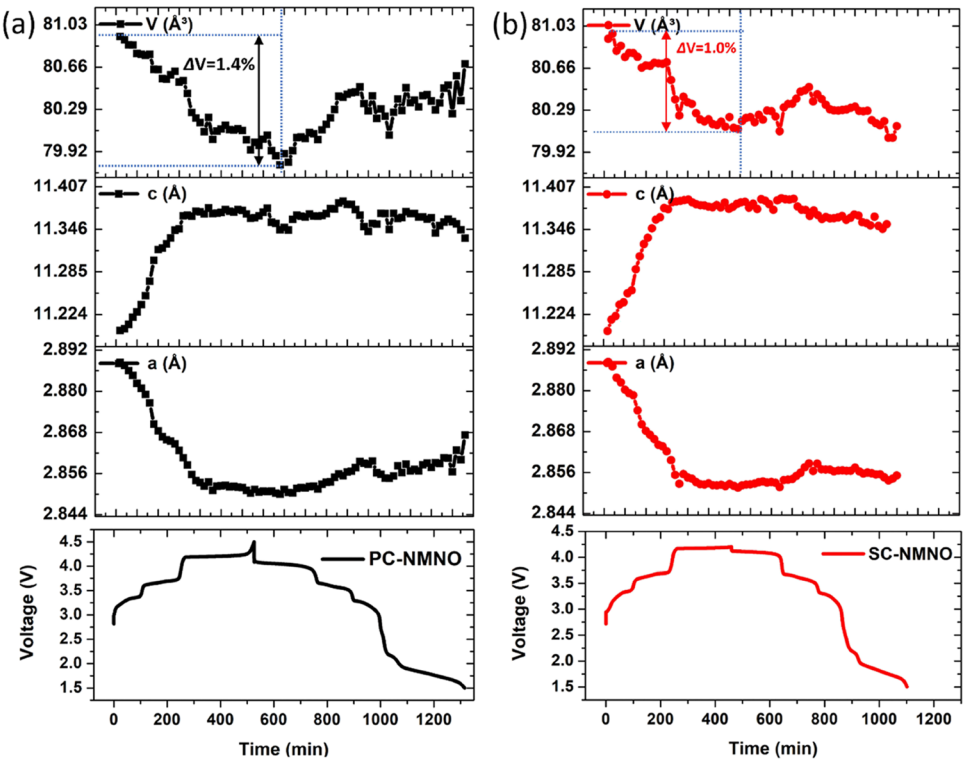

Figure 6. Variations in lattice parameters (for P2 phase) *a*, *c*, and unit-cell volume (*V*) for the first charge−discharge cycle during operando XRD for both PC and SC samples corresponding to Figures 5 and S7. (a) PC-NMNO and (b) SC-NMNO. Bottom to top: charge−discharge profile and *a*, *c*, and *V* variations. Lattice parameter evolutions for P2′ phase are shown in SI (Figure S8).

3.2.1. Capacity Fading Mechanisms. The rapid capacity fade in PC-NMNO could be caused by several phenomena such as particle cracking due to anisotropic volume changes,[7] exfoliation of the layered structure,[13] and/or irreversible oxygen redox reactions.[40,41] The total charge on the cathodes (considering ICP-OES data for both PC-NMNO and SC-NMNO) is between 3.37 and 3.16, which means a large amount of oxygen vacancies are present in them. It was well understood from the literature that such oxygen vacancies could lead to oxygen loss from the particle surface and can cause phase transformations and particle cracking, ultimately leading to poor performance.[42] To verify the presence of phase transformations and the associated volume changes as well as to gain more insight into the sodium storage mechanism and the phase evolution, operando XRD was performed on samples of both materials during the initial two charge−discharge cycles.

As shown in Figure 5 (SC-NMNO) and Figure S8 (PC-NMNO), both electrodes exhibited similar sodium storage and phase evolution behavior. First, upon charging, (002) and (004) reflections shifted to lower angles, while the rest of the reflections, for example (100), (102), (103), and (104), shifted to higher angles. It indicates the expansion and contraction of the *d* spacing, respectively. However, during the high voltage plateau at ∼4.16 V (at the end of charge and beginning of discharge), the positions of all of the reflections remained constant. While NMNO is known to exhibit P2 to O2 transformation in the high voltage region due to the structural instabilities,[8,10] there were no traces or additional peaks corresponding to such Z/OP4/O2 peaks, contrary to the literature.[43] The Z and OP4 phases are intergrowth structures between P2 and O2 type structures. Upon discharging, initially, a symmetrically opposite behavior was observed. Both electrodes demonstrated high reversibility, as is also seen from the similar peak evolution during the second cycle. Nevertheless, in the deep-discharged state i.e, ∼2−1.5 V, both electrodes showed a slightly more complex behavior corresponding to a biphasic region involving the P2-type hexagonal phase and a newly evolved P2′ orthorhombic phase (see the dotted black circle, Figure 5c). This P2′ phase is a distorted form of the P2 structure, which is usually observed in Mn-rich compounds owing to increased amount of Mn^{3+} ions in the deep-discharged state (i.e., Jahn−Teller distortion).[44] There is a noticeable difference in the degree of expansion or contraction of the (002) plane for both electrodes.

To verify this, lattice parameters were calculated for both electrodes during the first charge−discharge cycle and presented in Figure 6a,b. Upon charging to 4.2 V, lattice parameter *a* of both PC-NMNO and SC-NMNO electrodes decreased quickly and remained almost constant at the end of the charge. In contrast, *c* parameter increased quickly and remained almost constant at the end of charge.[45] During discharge, both *a* and *c* parameters did not display a variation tendency opposite that observed during charge, indicating a form of irreversibility of the lattice parameter evolution. This could be potentially related to the structural changes (Na^+/vacancy ordering or P2′ phase) observed in these electrodes. The calculated lattice parameters associated with the P2′ phase are presented in SI (Figure S9). However, the volume variations of both electrodes are considerably different from each other in the charged state. The percentage change in unit-cell volume *V* of SC-NMNO (Figure 6b) between open circuit voltage (OCV) and charge (4.2 V) is $\Delta V \sim 1.0\%$, which is lower than that of PC-NMNO ($\Delta V \sim 1.4\%$) (Figure 6a).

https://doi.org/10.1021/acsami.3c15348
ACS Appl. Mater. Interfaces 2024, 16, 25953−25965

Additionally, considering the P2′ phase transition during the discharge state, the volume variation of SC-NMNO (Figure S8) is $\Delta V \sim 1.7\%$, which is slightly lower than that of PC-NMNO ($\Delta V \sim 1.8\%$). It can be understood that, even though these volume changes are not significant, PC-NMNO is more vulnerable to particle microcracking than SC-NMNO, due to the presence of more grain boundaries (i.e., more anisotropic strain), which could eventually lead to poor interfacial stability and electrochemical performance of PC-NMNO. Nevertheless, these volume variations are comparable to the so-called "zero-strain" cathodes (volume changes <1%) in the literature.[45−49]

Additionally, the high surface area of PC-NMNO could facilitate electrolyte decomposition and dry-out and could be a further reason for capacity fading. The higher surface area facilitates several parasitic side reactions between the electrode and electrolyte during cycling, thereby leading to its decomposition.[50] Even though both electrodes predominantly retained their initial P2-type structure after cycling (see Figure 7a), noticeable differences were observed in particle morphology as shown in Figure 7b, c. The particle surfaces in the cycled electrode of PC-NMNO showed decomposition products (or surface degradation), indicated by rough surfaces.

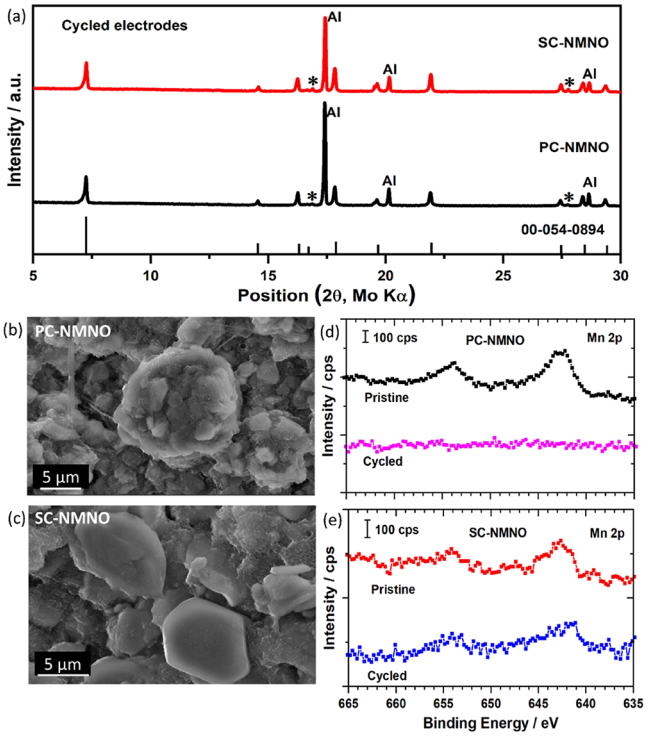

Figure 7. Postmortem analysis of cycled electrodes. (a) XRD patterns of cycled electrodes (the '*' peaks belong to an unknown phase), (b, c) SEM images of cycled PC-NMNO and SC-NMNO electrodes, respectively, and (d, e) XPS detail spectra in the Mn 2p region of pristine and cycled electrodes.

In contrast, the smooth surfaces of SC-NMNO particles indicate fewer degradation/decomposition products. Moreover, the absence of any Mn 2p signal in the XPS detail spectrum (Figure 7d) of the cycled PC-NMNO electrode also supports this assumption, indicating a relatively thick layer of electrolyte decomposition products such as metal fluorides and/or metal chlorides on the particle surface (see Figure S10). In contrast, the cycled electrode of SC-NMNO still shows the Mn 2p signal (Figure 6e), almost with the same intensity as that of the pristine electrode. Moreover, EDX mappings of cycled electrodes also show stronger F and Cl signals (corresponding to electrolyte decomposition products) in PC-NMNO compared to SC-NMNO (Figures S11 and S12), hence, a higher degree of decomposition at the former one. Additionally, SC-NMNO cathode materials possess low surface area, and due to the absence of grain boundaries, they exhibit high mechanical rigidity, which helps in suppressing/reducing crack formation during cycling. Even though the cycled electrodes of both samples did not show obvious particle cracks, it is believed that the SC particles exhibit higher resistance to particle cracking upon long-term cycling.[19,20]

Postmortem inspection found that the PC-NMNO delaminated from the current collector (see Figure S13), whereas the SC-NMNO electrode remained intact. This could be related to anisotropic volume changes in with PC-NMNO electrode, triggering the electrical isolation and the detachment of the electrode layer from the current collector.[51] For example, we observed in a previous study,[22] that PC-NMMO (synthesized at 900 °C) displayed a higher degree of particle cracking at different voltage windows compared to SC-NMMO (synthesized at 1100 °C). It seems plausible that PC-NMNO also behaves in a similar manner upon long-term cycling.

With respect to their thermal properties, SC-NMNO displayed ∼5% lower weight loss (Figure S14a) and significantly lower exothermic heat evolution around 400 °C (Figure S14b) compared to PC-NMNO, suggesting higher thermal stability of SC-NMNO that could enhance the safety and mitigate thermal runaway reactions.

3.2.2. Role of Aqueous Binders. The use of aqueous binders is limited in cathode electrode manufacturing due to the chemical incompatibility of many Li- and Na-ion battery cathode materials with water. Recently, there has been a growing interest in the aqueous processing of positive electrodes of LIBs to reduce manufacturing costs as well as to develop sustainable manufacturing processes.[30] In this study, since both cathode materials exhibited good air and water stability, PC-NMNO was taken as a reference cathode for aqueous electrode processing. The electrochemical performance of PC-NMNO electrodes with two different aqueous binders, namely, CMC and STMP, was evaluated and compared with PVDF-based electrodes (Figure 8). CMC-based binders are already commercially used in graphite anodes for Li-ion batteries.[30] STMP is a relatively new inorganic aqueous binder exhibiting excellent thermal properties and electrochemical performance.[52−56]

The PC-NMNO-CMC electrode exhibited a reversible capacity of 228 mA h/g, which is higher than that of STMP- (208 mA h/g) and PVDF- (212 mA h/g) based electrodes (Figure 8a). There are no noticeable differences between the charge−discharge profiles of the aqueous binder-based electrodes compared to PVDF. All three electrodes exhibited three different plateaus, as explained above.

The PC-NMNO electrode with aqueous binders showed a rapid decrease in their capacity for the first few cycles at a 1C rate (Figure 8b). This might be due to the water processing of PC-NMNO, which promotes sodium/proton exchange during the first cycles. This leads to loss of sodium, which results in lower initial capacities.[35] In spite of this capacity loss, the CMC-based electrode exhibited the highest capacity among the three electrodes, whereas the STMP-based electrode exhibited a slightly lower capacity than the PVDF-based

https://doi.org/10.1021/acsami.3c15348
ACS Appl. Mater. Interfaces 2024, 16, 25953−25965

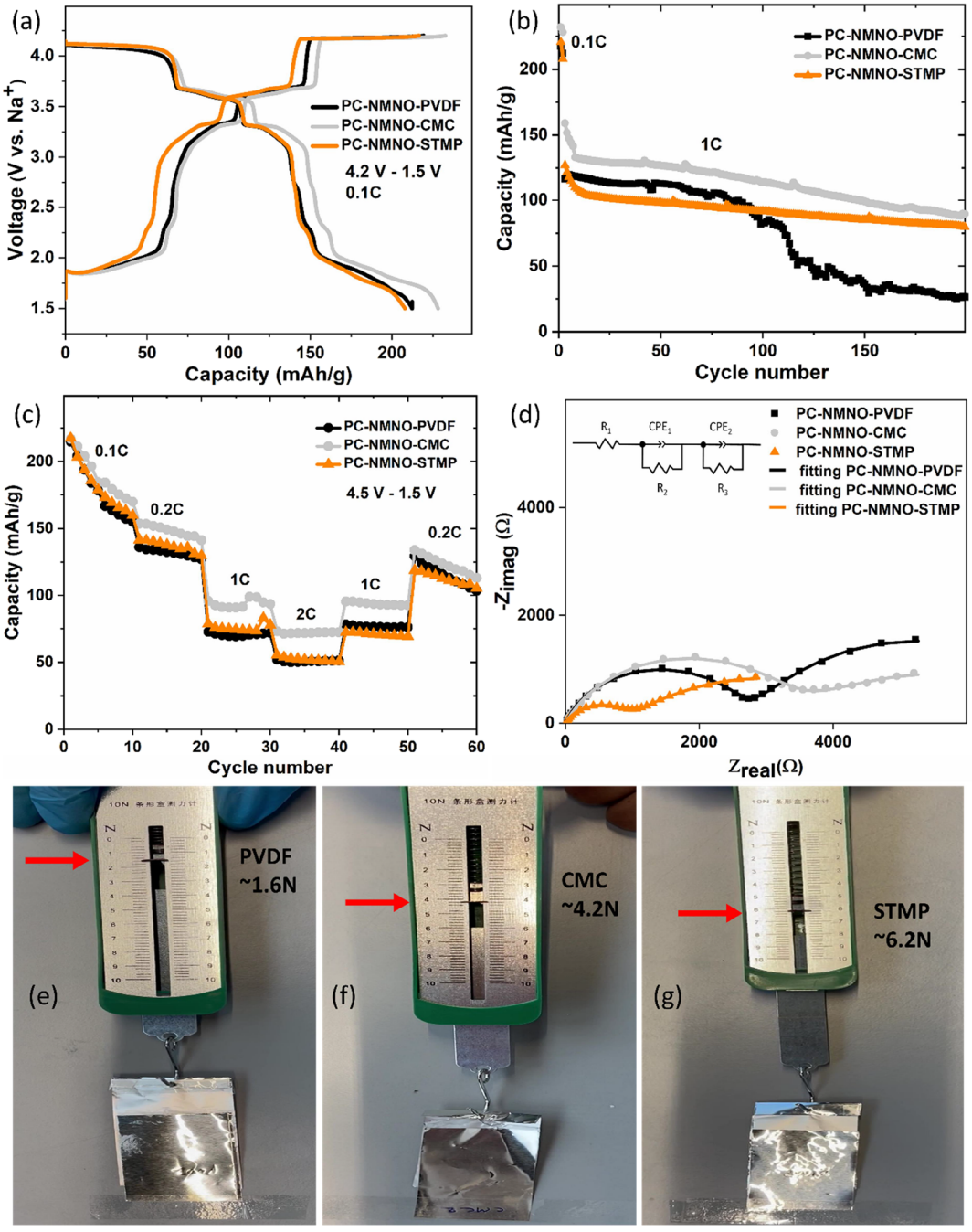

Figure 8. Electrochemical performance of PC-NMNO electrodes with different binders. (a) 2nd charge−discharge profiles at a rate of 0.1C, (b) cycling stability at 1C, (c) rate capability, and (d) electrochemical impedance spectra (EIS) (inset: electrochemical equivalent circuit). Binding strength results from peel-test experiments for (e) PVDF, (f) CMC, and (g) STMP binders.

electrode up to ~90 cycles. Afterward, the PVDF-based electrode faded rapidly for the above-mentioned reasons. At the same time, both CMC- and STMP-based electrodes continued to deliver high capacity, retaining 61 and 65% after 200 cycles, respectively, compared to 21% for the PVDF-based electrode.

We attribute improved cycling stability of aqueous binders compared to PVDF through a higher binding strength of the aqueous binders, as evident from Figure 8e−g. The binding strength of aqueous binders CMC (~4.2 N) and STMP (~6.2 N) is significantly higher than that of PVDF (~1.6 N) binder. Additionally, these aqueous binders are known to cover the active materials and carbon particles uniformly as a thin layer (acts as an artificial SEI) and provide protection against electrolyte attack and/or particle cracking.[51] While PVDF is a network-type binder, where the binding is largely based on weak van der Waals forces or physical interactions (mechanical interlocking).[57] The binding of CMC comes from the cross-linking of its functional groups with the substrate (chemical bonds).[58]

The binding ability of the inorganic aqueous binder STMP is a result of the condensation of its functional groups with the surface functional groups of electrode materials and substrates.[52,53] In addition, as shown in Figure 8c, the PC-NMNO electrode with the CMC binder exhibited slightly higher capacity at all rates, while STMP- and PVDF-based electrodes

https://doi.org/10.1021/acsami.3c15348
ACS Appl. Mater. Interfaces 2024, 16, 25953−25965

showed similar capacity. The improved electrochemical performance of CMC- and STMP-based electrodes was also supported by their reduced charge transfer resistance (R_{CT}) compared to PVDF (Figure 8d and Table S4). Overall, the aqueous binder-based electrodes exhibited enhanced electrochemical performance in terms of cycling stability and rate capability compared to the PVDF-based electrode. This could be attributed to the higher binding strength, uniform distribution of binder layer on the cathode/carbon particles as well as the improved kinetics resulting from the intrinsic ionic conductivity of CMC and STMP binders,[52,59] suggesting a great potential for positive electrode manufacturing. Especially, since STMP is a low-cost (significantly cheaper than PVDF and CMC), thermally stable, and water-soluble binder, battery manufacturing and recycling can be made substantially cheaper and sustainable.

4. CONCLUSIONS

Layered P2-type NMNO cathodes were synthesized as polycrystalline and single-crystalline particles to assess their physicochemical and electrochemical properties. Both PC-NMNO and SC-NMNO samples showed good bulk stability against air and water. The SC-NMNO exhibited ∼47% higher capacity retention than PC-NMNO after 175 cycles at 1C rate, which is attributed to the reduced surface area (leading to reduced parasitic side reactions or particle surface degradation) and suppressed microcracking of the particles (owing to the absence of grain boundaries) induced by the lower anisotropic volume variation of SC-NMNO ($\Delta V \sim 1.0\%$) compared to PC-NMNO ($\Delta V \sim 1.4\%$) upon charging to 4.2 V. According to the literature, such low volume changes of SC-NMNO make it nearly a "zero-strain" cathode material for sodium ion storage.

Comparably lower cycling stability of PC-NMNO is related to the electrolyte decomposition on the cathode particle surface, as well as the delamination of the electrode layer from the current collector. Additionally, PC-NMNO exhibited good electrochemical performance with aqueous binders, especially CMC, which exhibited higher capacity, better cycling stability (61% of initial capacity after 200 cycles at 1C rate), and rate capability. STMP-based electrodes delivered the highest capacity retention of ∼65% compared to ∼21% for PVDF after 200 cycles at 1C rate. The enhanced electrochemical performance of PC-NMNO with aqueous binders could be attributed to the higher binding strength, uniform distribution of the binder layer on the cathode/carbon particles, as well as the improved kinetics resulting from the intrinsic ionic conductivity of CMC and STMP binders. Looking at the future of the sustainable battery manufacturing landscape, NMNO forms a promising cathode material, and when processed with aqueous binders, the entire positive electrode manufacturing could potentially become cheaper, safer, and greener.

■ ASSOCIATED CONTENT

Supporting Information

The Supporting Information is available free of charge at https://pubs.acs.org/doi/10.1021/acsami.3c15348.

Experimental results; XRD, SEM, Raman spectroscopy, XPS, TGA, DSC, charge−discharge profiles; digital photographs of the cycled positive electrodes; and electrochemical performance comparison table from the literature (DOCX)

■ AUTHOR INFORMATION

Corresponding Authors

Venkat Pamidi − *Helmholtz Institute Ulm (HIU) Electrochemical Energy Storage, Ulm 89081, Germany;* orcid.org/0000-0002-9400-5456; Email: venkateshp.mme@gmail.com

Maximilian Fichtner − *Helmholtz Institute Ulm (HIU) Electrochemical Energy Storage, Ulm 89081, Germany; Institute of Nanotechnology (INT), Karlsruhe Institute of Technology (KIT), Karlsruhe 76021, Germany;* orcid.org/0000-0002-7127-1823; Email: m.fichtner@kit.edu

Authors

Carlos Naranjo − *Helmholtz Institute Ulm (HIU) Electrochemical Energy Storage, Ulm 89081, Germany*

Stefan Fuchs − *Helmholtz Institute Ulm (HIU) Electrochemical Energy Storage, Ulm 89081, Germany; Institute of Physical Chemistry (IPC), Karlsruhe Institute of Technology (KIT), Karlsruhe 76131, Germany;* orcid.org/0000-0001-8121-426X

Helge Stein − *Helmholtz Institute Ulm (HIU) Electrochemical Energy Storage, Ulm 89081, Germany; Institute of Physical Chemistry (IPC), Karlsruhe Institute of Technology (KIT), Karlsruhe 76131, Germany;* orcid.org/0000-0002-3461-0232

Thomas Diemant − *Helmholtz Institute Ulm (HIU) Electrochemical Energy Storage, Ulm 89081, Germany*

Yueliang Li − *Electron Microscopy Group of Materials Science, Ulm University, Ulm 89081, Germany*

Johannes Biskupek − *Electron Microscopy Group of Materials Science, Ulm University, Ulm 89081, Germany*

Ute Kaiser − *Electron Microscopy Group of Materials Science, Ulm University, Ulm 89081, Germany*

Sirshendu Dinda − *Helmholtz Institute Ulm (HIU) Electrochemical Energy Storage, Ulm 89081, Germany*

Adam Reupert − *Helmholtz Institute Ulm (HIU) Electrochemical Energy Storage, Ulm 89081, Germany*

Santosh Behara − *Faculty of Science and Engineering, Swansea University, Swansea SA1 8EN, United Kingdom*

Yang Hu − *Helmholtz Institute Ulm (HIU) Electrochemical Energy Storage, Ulm 89081, Germany;* orcid.org/0000-0001-6864-6498

Shivam Trivedi − *Helmholtz Institute Ulm (HIU) Electrochemical Energy Storage, Ulm 89081, Germany*

Anji Reddy Munnangi − *Faculty of Science and Engineering, Swansea University, Swansea SA1 8EN, United Kingdom;* orcid.org/0000-0001-9101-0252

Prabeer Barpanda − *Helmholtz Institute Ulm (HIU) Electrochemical Energy Storage, Ulm 89081, Germany; Faraday Materials Laboratory (FaMaL), Materials Research Centre, Indian Institute of Science, Bangalore 560012, India; Institute of Nanotechnology (INT), Karlsruhe Institute of Technology (KIT), Karlsruhe 76021, Germany;* orcid.org/0000-0003-0902-3690

Complete contact information is available at: https://pubs.acs.org/10.1021/acsami.3c15348

https://doi.org/10.1021/acsami.3c15348
ACS Appl. Mater. Interfaces 2024, 16, 25953−25965

Author Contributions

Conceptualization: V.P., methodology: V.P. and C.N., investigation: C.N., V.P., S.F., H.S., T.D., Y.L., S.G., J.B., U.K., S.D., A.R., S.B., Y.H., S.T., validation: V.P. and C.N., formal analysis: V.P. and C.N., resources: M.F., writing—original draft: V.P., visualization: V.P., writing—review and editing: M.A.R., P.B., and M.F., supervision: V.P., project administration: M.F., funding acquisition: M.F.

Notes

The authors declare no competing financial interest.

■ ACKNOWLEDGMENTS

This work contributes to the research performed at CELEST (Center for Electrochemical Energy Storage Ulm-Karlsruhe) and was funded by the German Research Foundation (DFG) under project ID 390874152 (POLiS Cluster of Excellence, EXC 2154). V.P. acknowledges the help of Dr. Bosubabu Dasari for TGA-DSC measurements and Ruochen Xu for postmortem analysis and lattice parameter calculations from operando XRD data. We are thankful to S. Grözinger for the TEM sample preparation. P.B. is grateful to the Alexander von Humboldt Foundation (Bonn, Germany) for a 2022 Humboldt fellowship for experienced researchers. This project received funding from the European Union's Horizon 2020 research and innovation program under grant agreement No. 957189. The authors acknowledge BATTERY 2030PLUS funded by the European Union's Horizon 2020 research and innovation program under Grant Agreement No. 957213.

■ REFERENCES

(1) Tapia-Ruiz, N.; Armstrong, A. R.; Alptekin, H.; Amores, M. A.; Au, H.; Barker, J.; Boston, R.; Brant, W. R.; Brittain, J. M.; Chen, Y.; Chhowalla, M.; Choi, Y. S.; Costa, S. I. R.; Ribadeneyra, M. C.; Cussen, S. A.; Cussen, E. J.; David, W. I. F.; Desai, A. V.; Dickson, S. A. M.; Eweka, E. I.; Forero-Saboya, J. D.; Grey, C. P.; Griffin, J. M.; Gross, P.; Hua, X.; Irvine, J. T. S.; Johansson, P.; Jones, M. O.; Karlsmo, M.; Kendrick, E.; Kim, E.; Kolosov, O. V.; Li, Z.; Mertens, S. F. L.; Mogensen, R.; Monconduit, L.; Morris, R. E.; Naylor, A. J.; Nikman, S.; O'Keefe, C. A.; Ould, D. M. C.; Palgrave, R. G.; Poizot, P.; Ponrouch, A.; Renault, S.; Reynolds, E. M.; Rudola, A.; Sayers, R.; Scanlon, D. O.; Sen, S.; Seymour, V. R.; Silván, B.; Sougrati, M. T.; Stievano, L.; Stone, G. S.; Thomas, C. I.; Titirici, M. M.; Tong, J.; Wood, T. J.; Wright, D. S.; Younesi, R. Roadmap for Sodium-Ion Batteries. *J. Phys.: Energy* **2021**, *3* (3), No. 031503.

(2) Hasa, I.; Mariyappan, S.; Saurel, D.; Adelhelm, P.; Koposov, A. Y.; Masquelier, C.; Croguennec, L.; Casas-Cabanas, M. Challenges of Today for Na-Based Batteries of the Future: From Materials to Cell Metrics. *J. Power Sources* **2021**, *482*, No. 228872.

(3) Lu, Z.; Dahn, J. R. In Situ X-Ray Diffraction Study of P2-Na[Sub 2/3][Ni[Sub 1/3]Mn[Sub 2/3]]O[Sub 2]. *J. Electrochem. Soc.* **2001**, *148* (11), A1225.

(4) Mao, J.; Liu, X.; Liu, J.; Jiang, H.; Zhang, T.; Shao, G.; Ai, G.; Mao, W.; Feng, Y.; Yang, W.; Liu, G.; Dai, K. P2-Type Na 2/3 Ni 1/3 Mn 2/3 O 2 Cathode Material with Excellent Rate and Cycling Performance for Sodium-Ion Batteries. *J. Electrochem. Soc.* **2019**, *166* (16), A3980−A3986.

(5) Pfeiffer, L. F.; Jobst, N.; Gauckler, C.; Lindén, M.; Marinaro, M.; Passerini, S.; Wohlfahrt-Mehrens, M.; Axmann, P. Layered P2-NaxMn3/4Ni1/4O2 Cathode Materials For Sodium-Ion Batteries: Synthesis, Electrochemistry and Influence of Ambient Storage. *Front Energy Res.* **2022**, *10* (May), 1−17.

(6) Kubota, K.; Komaba, S. Review—Practical Issues and Future Perspective for Na-Ion Batteries. *J. Electrochem. Soc.* **2015**, *162* (14), A2538−A2550.

(7) Wang, K.; Yan, P.; Sui, M. Phase Transition Induced Cracking Plaguing Layered Cathode for Sodium-Ion Battery. *Nano Energy* **2018**, *54*, 148−155.

(8) Wang, P. F.; You, Y.; Yin, Y. X.; Wang, Y. S.; Wan, L. J.; Gu, L.; Guo, Y. G. Suppressing the P2−O2 Phase Transition of Na0.67Mn0.67Ni0.33O2by Magnesium Substitution for Improved Sodium-Ion Batteries. *Angewandte Chemie - International Edition* **2016**, *55* (26), 7445−7449.

(9) Wang, H.; Gao, R.; Li, Z.; Sun, L.; Hu, Z.; Liu, X. Different Effects of Al Substitution for Mn or Fe on the Structure and Electrochemical Properties of Na0.67Mn0.5Fe0.5O2 as a Sodium Ion Battery Cathode Material. *Inorg. Chem.* **2018**, *57* (9), 5249−5257.

(10) Pahari, D.; Puravankara, S. On Controlling the P2-O2 Phase Transition by Optimal Ti-Substitution on Ni-Site in P2-Type Na0.67Ni0.33Mn0.67O2 (NNMO) Cathode for Na-Ion Batteries. *J. Power Sources* **2020**, *455*, No. 227957.

(11) Mu, L.; Xu, S.; Li, Y.; Hu, Y. S.; Li, H.; Chen, L.; Huang, X. Prototype Sodium-Ion Batteries Using an Air-Stable and Co/Ni-Free O3-Layered Metal Oxide Cathode. *Adv. Mater.* **2015**, *27* (43), 6928−6933.

(12) Hasa, I.; Buchholz, D.; Passerini, S.; Scrosati, B.; Hassoun, J. High Performance Na0.5[Ni0.23Fe0.13Mn0.63]O2 Cathode for Sodium-Ion Batteries. *Adv. Energy Mater.* **2014**, *4* (15), No. 201400083.

(13) Liu, Y.; Fang, X.; Zhang, A.; Shen, C.; Liu, Q.; Enaya, H. A.; Zhou, C. Layered P2-Na2/3[Ni1/3Mn2/3]O2 as High-Voltage Cathode for Sodium-Ion Batteries: The Capacity Decay Mechanism and Al2O3 Surface Modification. *Nano Energy* **2016**, *27*, 27−34.

(14) Yu, Y.; Kong, W.; Li, Q.; Ning, D.; Schuck, G.; Schumacher, G.; Su, C.; Liu, X. Understanding the Multiple Effects of TiO2 Coating on NaMn0.33Fe0.33Ni0.33O2 Cathode Material for Na-Ion Batteries. *ACS Appl. Energy Mater.* **2020**, *3* (1), 933−942.

(15) Kong, W.; Wang, H.; Sun, L.; Su, C.; Liu, X. Understanding the Synergic Roles of MgO Coating on the Cycling and Rate Performance of Na0.67Mn0.5Fe0.5O2 Cathode. *Appl. Surf. Sci.* **2019**, *497*, No. 143814.

(16) Jiao, J.; Wu, K.; Dang, R.; Li, N.; Deng, X.; Liu, X.; Hu, Z.; Xiao, X. A Collaborative Strategy with Ionic Conductive Na2SiO3 Coating and Si Doping of P2-Na0.67Fe0.5Mn0.5O2 Cathode: An Effective Solution to Capacity Attenuation. *Electrochim. Acta* **2021**, *384*, No. 138362.

(17) Chen, C.; Han, Z.; Chen, S.; Qi, S.; Lan, X.; Zhang, C.; Chen, L.; Wang, P.; Wei, W. Core-Shell Layered Oxide Cathode for High-Performance Sodium-Ion Batteries. *ACS Appl. Mater. Interfaces* **2020**, *12* (6), 7144−7152.

(18) Yang, L.; del Amo, J. M. L.; Shadike, Z.; Bak, S. M.; Bonilla, F.; Galceran, M.; Nayak, P. K.; Buchheim, J. R.; Yang, X. Q.; Rojo, T.; Adelhelm, P. A Co- and Ni-Free P2/O3 Biphasic Lithium Stabilized Layered Oxide for Sodium-Ion Batteries and Its Cycling Behavior. *Adv. Funct Mater.* **2020**, *30* (42), 1−11.

(19) Li, J.; Cameron, A. R.; Li, H.; Glazier, S.; Xiong, D.; Chatzidakis, M.; Allen, J.; Botton, G. A.; Dahn, J. R. Comparison of Single Crystal and Polycrystalline LiNi 0.5 Mn 0.3 Co 0.2 O 2 Positive Electrode Materials for High Voltage Li-Ion Cells. *J. Electrochem. Soc.* **2017**, *164* (7), A1534−A1544.

(20) Qian, G.; Zhang, Y.; Li, L.; Zhang, R.; Xu, J.; Cheng, Z.; Xie, S.; Wang, H.; Rao, Q.; He, Y.; Shen, Y.; Chen, L.; Tang, M.; Ma, Z. F. Single-Crystal Nickel-Rich Layered-Oxide Battery Cathode Materials: Synthesis, Electrochemistry, and Intra-Granular Fracture. *Energy Storage Mater.* **2020**, *27*, 140−149.

(21) Klein, S.; Bärmann, P.; Fromm, O.; Borzutzki, K.; Reiter, J.; Fan, Q.; Winter, M.; Placke, T.; Kasnatscheew, J. Prospects and Limitations of Single-Crystal Cathode Materials to Overcome Cross-Talk Phenomena in High-Voltage Lithium Ion Cells. *J. Mater. Chem. A Mater.* **2021**, *9* (12), 7546−7555.

(22) Pamidi, V.; Trivedi, S.; Behara, S.; Fichtner, M.; Reddy, M. A. Micron-Sized Single-Crystal Cathodes for Sodium-Ion Batteries. *iScience* **2022**, *25* (5), No. 104205.

https://doi.org/10.1021/acsami.3c15348
ACS Appl. Mater. Interfaces 2024, 16, 25953−25965

(23) Yang, L.; Chen, C.; Xiong, S.; Zheng, C.; Liu, P.; Ma, Y.; Xu, W.; Tang, Y.; Ong, S. P.; Chen, H. Multiprincipal Component P2-Na 0.6 (Ti 0.2 Mn 0.2 Co 0.2 Ni 0.2 Ru 0.2)O 2 as a High-Rate Cathode for Sodium-Ion Batteries. *JACS Au* **2021**, *1* (1), 98−107.
(24) Su, D.; Wang, C.; Ahn, H. J.; Wang, G. Single Crystalline Na0.7MnO2 Nanoplates as Cathode Materials for Sodium-Ion Batteries with Enhanced Performance. *Chem.—Eur. J.* **2013**, *19* (33), 10884−10889.
(25) Chen, T.; Fan, X.; Zhuo, Y.; Ouyang, B.; Chen, X.; Liu, K. A Monocrystalline Orthorhombic Na0.44Mn0.9Li0.1O2cathode with Outstanding Stability and Negligible Structural Strain for Sodium-Ion Batteries. *Inorg. Chem. Front* **2021**, *8* (11), 2844−2853.
(26) Yuan, S.; Liu, Y. B.; Xu, D.; Ma, D. L.; Wang, S.; Yang, X. H.; Cao, Z. Y.; Zhang, X. B. Pure Single-Crystalline Na1.1V3O7.9 Nanobelts as Superior Cathode Materials for Rechargeable Sodium-Ion Batteries. Advanced. *Science* **2015**, *2* (3), 1−6.
(27) Chen, H.; Ling, M.; Hencz, L.; Ling, H. Y.; Li, G.; Lin, Z.; Liu, G.; Zhang, S. Exploring Chemical, Mechanical, and Electrical Functionalities of Binders for Advanced Energy-Storage Devices. *Chem. Rev.* **2018**, *118* (18), 8936−8982.
(28) Zhu, W.; Schmehl, D. R.; Mullin, C. A.; Frazier, J. L. Four Common Pesticides, Their Mixtures and a Formulation Solvent in the Hive Environment Have High Oral Toxicity to Honey Bee Larvae. *PLoS One* **2014**, *9* (1), No. e77547.
(29) Wood, D. L.; Quass, J. D.; Li, J.; Ahmed, S.; Ventola, D.; Daniel, C. Technical and Economic Analysis of Solvent-Based Lithium-Ion Electrode Drying with Water and NMP. *Drying Technology* **2018**, *36* (2), 234−244.
(30) Liu, Y.; Zhang, R.; Wang, J.; Wang, Y. Current and Future Lithium-Ion Battery Manufacturing. *iScience* **2021**, *24* (4), No. 102332.
(31) Stein, H. S.; Sanin, A.; Rahmanian, F.; Zhang, B.; Vogler, M.; Flowers, J. K.; Fischer, L.; Fuchs, S.; Choudhary, N.; Schroeder, L. From Materials Discovery to System Optimization by Integrating Combinatorial Electrochemistry and Data Science. *Curr. Opin Electrochem* **2022**, *35*, No. 101053.
(32) Langdon, J.; Manthiram, A. A Perspective on Single-Crystal Layered Oxide Cathodes for Lithium-Ion Batteries. *Energy Storage Mater.* **2021**, *37*, 143−160.
(33) Delmas, C.; Fouassier, C.; Hagenmuller, P. Structural Classification and Properties of the Layered Oxides. *Physica B+C* **1980**, *99* (1−4), 81−85.
(34) Gutierrez, A.; Dose, W. M.; Borkiewicz, O.; Guo, F.; Avdeev, M.; Kim, S.; Fister, T. T.; Ren, Y.; Bareño, J.; Johnson, C. S. On Disrupting the Na+-Ion/Vacancy Ordering in P2-Type Sodium-Manganese-Nickel Oxide Cathodes for Na+-Ion Batteries. *J. Phys. Chem. C* **2018**, *122* (41), 23251−23260.
(35) Zuo, W.; Qiu, J.; Liu, X.; Ren, F.; Liu, H.; He, H.; Luo, C.; Li, J.; Ortiz, G. F.; Duan, H.; Liu, J.; Wang, M. S.; Li, Y.; Fu, R.; Yang, Y. The Stability of P2-Layered Sodium Transition Metal Oxides in Ambient Atmospheres. *Nat. Commun.* **2020**, *11* (1), 1−12.
(36) Xu, C.; Cai, H.; Chen, Q.; Kong, X.; Pan, H.; Hu, Y. S. Origin of Air-Stability for Transition Metal Oxide Cathodes in Sodium-Ion Batteries. *ACS Appl. Mater. Interfaces* **2022**, *14* (4), 5338−5345.
(37) Zuo, W.; Innocenti, A.; Zarrabeitia, M.; Bresser, D.; Yang, Y.; Passerini, S. Layered Oxide Cathodes for Sodium-Ion Batteries: Storage Mechanism, Electrochemistry, and Techno-Economics. *Acc. Chem. Res.* **2023**, *56* (3), 284−296.
(38) Zuo, W.; Xiao, Z.; Zarrabeitia, M.; Xue, X.; Yang, Y.; Passerini, S. Guidelines for Air-Stable Lithium/Sodium Layered Oxide Cathodes. *ACS Mater. Lett.* **2022**, *4*, 1074−1086.
(39) Nakayama, M.; Konishi, S.; Tagashira, H.; Ogura, K. Electrochemical Synthesis of Layered Manganese Oxides Intercalated with Tetraalkylammonium Ions. *Langmuir* **2005**, *21* (1), 354−359.
(40) Zhang, Y.; Wu, M.; Ma, J.; Wei, G.; Ling, Y.; Zhang, R.; Huang, Y. Revisiting the Na2/3Ni1/3Mn2/3O2 Cathode: Oxygen Redox Chemistry and Oxygen Release Suppression. *ACS Cent Sci.* **2020**, *6* (2), 232−240.
(41) Ma, C.; Alvarado, J.; Xu, J.; Clément, R. J.; Kodur, M.; Tong, W.; Grey, C. P.; Meng, Y. S. Exploring Oxygen Activity in the High Energy P2-Type Na0.78Ni0.23Mn0.69O2 Cathode Material for Na-Ion Batteries. *J. Am. Chem. Soc.* **2017**, *139* (13), 4835−4845.
(42) Tang, Z. K.; Xue, Y. F.; Teobaldi, G.; Liu, L. M. The Oxygen Vacancy in Li-Ion Battery Cathode Materials. *Nanoscale Horiz.* **2020**, *5*, 1453−1466, DOI: 10.1039/d0nh00340a.
(43) Somerville, J. W.; Sobkowiak, A.; Tapia-Ruiz, N.; Billaud, J.; Lozano, J. G.; House, R. A.; Gallington, L. C.; Ericsson, T.; Häggström, L.; Roberts, M. R.; Maitra, U.; Bruce, P. G. Nature of the "Z"-Phase in Layered Na-Ion Battery Cathodes. *Energy Environ. Sci.* **2019**, *12* (7), 2223−2232.
(44) Mortemard de Boisse, B.; Carlier, D.; Guignard, M.; Bourgeois, L.; Delmas, C. P2-Na x Mn 1/2 Fe 1/2 O 2 Phase Used as Positive Electrode in Na Batteries: Structural Changes Induced by the Electrochemical (De)Intercalation Process. *Inorg. Chem.* **2014**, *53* (20), 11197−11205.
(45) Hua, W.; Yang, X.; Wang, S.; Li, H.; Senyshyn, A.; Tayal, A.; Baran, V.; Chen, Z.; Avdeev, M.; Knapp, M.; Ehrenberg, H.; Saadoune, I.; Chou, S.; Indris, S.; Guo, X. Dynamic Inconsistency between Electrochemical Reaction and Phase Transition in Na-Deficient Layered Cathode Materials. *Energy Storage Mater.* **2023**, *61*, No. 102906.
(46) Yang, X.; Wang, S.; Li, H.; Peng, J.; Zeng, W. J.; Tsai, H. J.; Hung, S. F.; Indris, S.; Li, F.; Hua, W. Boosting the Ultrastable High-Na-Content P2-Type Layered Cathode Materials with Zero-Strain Cation Storage via a Lithium Dual-Site Substitution Approach. *ACS Nano* **2023**, *17* (18), 18616−18628.
(47) Zhao, X.; Ceder, G. Zero-Strain Cathode Materials for Li-Ion Batteries. *Joule* **2022**, *6*, 2683−2685.
(48) Zhang, R.; Wang, C.; Zou, P.; Lin, R.; Ma, L.; Yin, L.; Li, T.; Xu, W.; Jia, H.; Li, Q.; Sainio, S.; Kisslinger, K.; Trask, S. E.; Ehrlich, S. N.; Yang, Y.; Kiss, A. M.; Ge, M.; Polzin, B. J.; Lee, S. J.; Xu, W.; Ren, Y.; Xin, H. L. Compositionally Complex Doping for Zero-Strain Zero-Cobalt Layered Cathodes. *Nature* **2022**, *610* (7930), 67−73.
(49) Park, S. H.; Lee, N. K.; Lee, S. G.; Han, J. H.; Lee, Y. J. Zero-Strain Cathodes for Lithium-Based Rechargeable Batteries: A Comprehensive Review. *ACS Appl. Energy Mater.* **2023**, *6*, 12−30.
(50) Wang, P. F.; Yao, H. R.; Liu, X. Y.; Yin, Y. X.; Zhang, J. N.; Wen, Y.; Yu, X.; Gu, L.; Guo, Y. G. Na+/Vacancy Disordering Promises High-Rate Na-Ion Batteries. *Sci. Adv.* **2018**, *4* (3), 1−10.
(51) Yoda, Y.; Kubota, K.; Isozumi, H.; Horiba, T.; Komaba, S. Poly-γ-Glutamate Binder to Enhance Electrode Performances of P2-Na2/3Ni1/3Mn2/3O2 for Na-Ion Batteries. *ACS Appl. Mater. Interfaces* **2018**, *10* (13), 10986−10997.
(52) Trivedi, S.; Pamidi, V.; Fichtner, M.; Anji Reddy, M. Ionically Conducting Inorganic Binders: A Paradigm Shift in Electrochemical Energy Storage. *Green Chem.* **2022**, *24* (14), 5620−5631.
(53) Wei, C.; Obrovac, M. N. Inorganic Compounds as Binders for Si-Alloy Anodes. *J. Electrochem. Soc.* **2021**, *168* (2), No. 020505.
(54) Trivedi, S.; Dinda, S.; Tang, Y.; Fuchs, S.; Pamidi, V.; Stein, H. S.; Munnangi, A. R.; Fichtner, M. SiOx Coated Graphite with Inorganic Aqueous Binders as High-Performance Anode for Lithium-Ion Batteries. *J. Energy Storage* **2023**, *71*, No. 109210.
(55) Trivedi, S.; Pamidi, V.; Bautista, S. P.; Shamsudin, F. N. A.; Weil, M.; Barpanda, P.; Bresser, D.; Fichtner, M. Water-Soluble Inorganic Binders for Lithium-Ion and Sodium-Ion Batteries. *Adv. Energy Mater.* **2024**, *14*, No. 2303338, DOI: 10.1002/aenm.202303338.
(56) Xu, R.; Pamidi, V.; Tang, Y.; Fuchs, S.; Stein, H.; Dasari, B.; Zhao-Karger, Z.; Behara, S.; Hu, Y.; Trivedi, S.; Munnangi, A. R.; Barpanda, P.; Fichtner, M. Greener, Safer and Better Performing Aqueous Binder for Positive Electrode Manufacturing of Sodium Ion Batteries. *ChemSusChem* **2024**, No. e202301154, DOI: 10.1002/cssc.202301154.
(57) Zhong, X.; Han, J.; Chen, L.; Liu, W.; Jiao, F.; Zhu, H.; Qin, W. Binding Mechanisms of PVDF in Lithium Ion Batteries. *Appl. Surf. Sci.* **2021**, *553*, No. 149564.

(58) Lestriez, B.; Bahri, S.; Sandu, I.; Roué, L.; Guyomard, D. On the Binding Mechanism of CMC in Si Negative Electrodes for Li-Ion Batteries. *Electrochem commun* **2007**, *9* (12), 2801−2806.
(59) Xie, L.; Zhao, L.; Wan, J.; Shao, Z.; Wang, F.; Lv, S. The Electrochemical Performance of Carboxymethyl Cellulose Lithium as a Binding Material for Anthraquinone Cathodes in Lithium Batteries. *J. Electrochem. Soc.* **2012**, *159* (4), A499−A505.

https://doi.org/10.1021/acsami.3c15348
ACS Appl. Mater. Interfaces 2024, 16, 25953−25965